HiSST: 2nd International Conference on High-Speed Vehicle Science & Technology

11–15 September 2022, Bruges, Belgium

Influence of the rarefaction degree on the aerodynamic performances of hypersonic waveriders: experimental and numerical analysis

Damien Toussaint[1], *Jean-Philippe Braeunig*[2], *Céline Baranger*[3], *Hugo Noubel*[4], *Viviana Lago*[5]

Abstract

Waveriders are a concept of hypersonic lifting vehicles designed to generate an attached bow shock at its leading edge. Even though this concept is a very active research topic, very little experimental campaigns were conducted, especially to assess viscous influence on waverider performance. To compensate for this lack of experimental data, CNRS/ICARE performed an experimental investigation of the aerodynamic performances of waveriders in rarefied supersonic flows, with Mach numbers ranging from to 2 to 4 and Knudsen number from 8.3×10^{-5} to 2.1×10^{-3}. In the present study, these experimental data are compared with numerical results of simulations performed with a Navier-Stokes, a discrete-ordinate ES-BGK and a DSMC solvers for validation purpose. These numerical computations are then used to complement the experimental observations.

Keywords: *Waverider, Super-/Hypersonic flow, Rarefied flow, ES-BGK, DSMC*

Nomenclature

Latin

D – Drag force
f – Mass distribution function
f_{num} – Ratio of physical particles to numerical particles
$\mathcal{G}$ – Gaussian distribution function
Kn – Knudsen number
L – Lift force
L/D – Lift to drag ratio
$\mathcal{M}$ – Maxwellian distribution function
Ma – Mach number
N_{part} – Number of particles
$N_{p/c}$ – Number of particles per cell
N_ρ – Particle density
Pr – Prandtl number
p – Pressure
Re – Reynolds number
T – Temperature
T_w – Wall temperature
u – Flow velocity
x – Longitudinal coordinate
y – Normal coordinate
z – Transversal coordinate
Z_{rot} – Rotation number

Greek

α – Angle of attack
α_{acc} – Parietal accommodation coefficient
Δt – Simulation time step
ρ – Density
τ_{coll} – Collision time

[1]*CEA-Cesta, 15 avenue des Sablières – CS 60001, 33116 Le Barp Cedex, France, damien.toussaint@cea.fr*
[2]*CEA-Cesta, 15 avenue des Sablières – CS 60001, 33116 Le Barp Cedex, France, jean-philippe.braeunig@cea.fr*
[3]*CEA-Cesta, 15 avenue des Sablières – CS 60001, 33116 Le Barp Cedex, France, celine.baranger@cea.fr*
[4]*CNRS/ICARE, 1c avenue de la Recherche Scientifique, CS 50060, F-45071, Orléans Cedex 2, France, hugo.noubel@cnrs-orleans.fr*
[5]*CNRS/ICARE, 1c avenue de la Recherche Scientifique, CS 50060, F-45071, Orléans Cedex 2, France, Viviana.lago@cnrs-orleans.fr*

1. Introduction

Since its introduction by Nonweiler [1] in 1959, the concept of waverider is a very active research topic (see for instance the works of Jones, Bowcutt, Anderson, Rasmussen... and co-workers). A waverider is a super-/hypersonic lifting vehicle with an attached (or nearly attached) bow shock at its leading edge. It thus appears to ride on the top of the shock wave. In this way, waveriders produce higher lift than generic hypersonic vehicles at a given angle of attack (AoA) and generate higher lift-to-drag ratios (L/D) for the same produced lift. Due to their superior aerodynamic characteristics, waveriders are regarded as strong candidates for long-range re-entry vehicles capable of carrying payload.

Therefore, these vehicles are expected to fly at very high speeds (Mach number up to 10-15) and high altitudes, especially above 60 km where the gas flow is no longer continuous but rarefied. The rarefaction degree of the flow may significantly influence the aerodynamic properties of such vehicles, mainly due to strong viscous interaction that may induce the detachment of the shock from the leading edge. Although some numerical studies assessed these flow rarefaction's effects, very little experimental campaigns were conducted to support these findings to the knowledge of the authors. This lack of experimental data and experimental/numerical confrontation motivates the present study.

The present work actually results from the collaboration between CNRS/ICARE and CEA-Cesta, which decided to combine their respective expertise in experimental observations and numerical simulation/modelling of rarefied flows. This collaboration aims at taking profit of the experimental measurements performed within the framework of the APHYRA project for solvers validation and rarefied flow modelling purposes. This in-progress project, leaded by CNRS/ICARE and funded by the French Research National Agency (ANR), aims at assessing the rarefaction effects on waveriders' aerodynamic properties by experimental means.

These experimental data are not only expected to provide a better understanding of the rarefied aerodynamics properties of waveriders, but they also represent a very rare and valuable database to validate numerical solvers and improve their accuracy. In the present work, numerical simulations are performed with the three super-/hypersonic solvers generally used at CEA: the in-house NS solver that resolves the Navier-Stokes equations, the in-house K solver which provides a steady-state solution for the ES-BGK models' equations using a discrete-ordinate deterministic approach and the open-source SPARTA solver, designed to solve the Boltzmann equation using the DSMC algorithm of Bird [2].

The present paper is therefore organised as follows. First, the principles of waverider design are concisely described in Sec. 2. Then the experimental and numerical methodology is detailed in Sec. 3. Comparisons between numerical and experimental results are performed in Sec. 4, and further results are introduced. Finally, the main findings and perspectives of this work are summarised in Sec. 5.

2. Principle of waverider design

As mentioned in Sec. 1, a waverider is a supersonic or hypersonic vehicle with an attached bow shock all along its leading edge (LE). This feature is in contrast with generic vehicles, for which the shock is mainly detached from the LE (see fig. 1a–1b). Waveriders therefore appear to ride over the shock wave and the zone of high pressure under the vehicle does not leak to the top surface, leading to higher lift force than generic vehicle for a given angle of attack (AoA). The wave drag is also strengthened such that the lift-to-drag (L/D) ratio of waveriders is only slightly improved compared to generic vehicles. However, for a given lift force, generic vehicle must fly at higher AoA than waveriders, thus inducing higher drag. Therefore, the L/D ratio of waveriders is significantly increased compared to classical vehicles for a given lift force (see fig. 1c). This property stands as the main advantage of waveriders.

A waverider is generally designed from a supersonic or hypersonic flowfield around a simple shape. The conical flowfield, illustrated in fig. 1b and used to design the waverider of the present study, is the most widespread configuration [3]. This flowfield is generated by a cone at 0° AoA. The leading edge of the resulting waverider is defined arbitrarily on the shock. In this manner, the shock will be attached all along the LE. Any streamsurface delimited by this LE curve can be considered as a surface of the

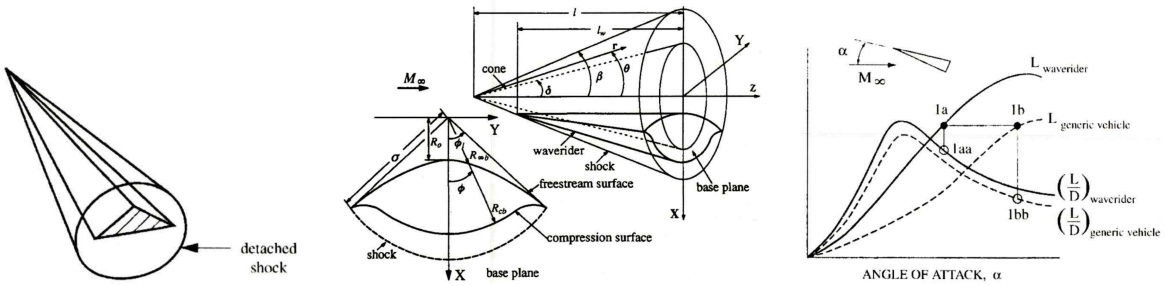

(a) Generic vehicle [4]

(b) Cone-derived waverider construction [5]

(c) Comparison of L/D ratio between generic and waverider vehicle [5]

Fig 1. Comparison of generic and waverider vehicles.

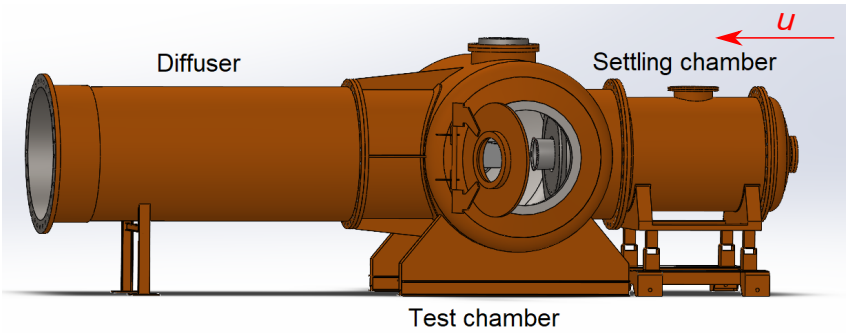

Fig 2. Schematic of the MARHy wind-tunnel [7].

waverider. Note that the resulting waverider is a point-design vehicle, i.e. designed for a given flow condition and AoA. More details concerning waverider design can be found in the review performed by Ding *et al.* [3].

3. Experimental and numerical methodology

3.1. Experimental details

The experiment is conducted in the low-density MARHy facility of CNRS/ICARE by H. Noubel and V. Lago [6] in the framework of the APHYRA ANR project. MARHy is a super-/hypersonic wind-tunnel enabling to reproduce rarefied slip and transition flow conditions. The wind-tunnel is illustrated in Fig. 2. The flow expands through a nozzle housed between the settling and the test chambers. A micro-valve enables to set the nozzle stagnation conditions. Downstream the test chamber, the diffuser is connected to a powerful pumping unit (with a vacuum capacity of 153000 $m^3\,h^{-1}$), enabling to maintain stabilised low pressure within the test chamber. Thanks to a set of curved- and contour-shaped nozzles, this facility covers a large range of Mach number (from 0.6 to 20.2) and pressure conditions within the test chamber (between 0.07 to 71 Pa). MARHy can operate continuously for several hours, which is suitable to stabilise the flow conditions before any experiment. The present study is conducted at Mach Ma $= 2$ with a static pressure of $p = 8$ Pa and Mach Ma $= 4$ – p = 2.67, 8, 71 Pa, enabling to perform at the same time iso-pressure and iso-Mach studies. The flow operating conditions are listed in Tab. 1. Note that the first line of the table corresponds to the name of the nozzles, which are a concatenation of the Mach number and the static pressure in the test section.

The studied waverider is inspired by the work of Rolim *et al.* [8] and was adapted by CNRS/ICARE to

Table 1. MARHy operating conditions.

M2-8Pa	M4-2.67Pa	M4-8Pa	M4-71Pa
p = 7.99 Pa	p = 2.67 Pa	p = 7.99 Pa	p = 71.1 Pa
T = 162.78 K	T = 69.76 K	T = 69.76 K	T = 69.76 K
ρ = 1.71×10^{-4} kg/m^3	ρ = 1.33×10^{-4} kg/m^3	ρ = 3.99×10^{-4} kg/m^3	ρ = 3.55×10^{-3} kg/m^3
u = 511.4 m/s	u = 669.6 m/s	u = 669.6 m/s	u = 669.6 m/s
Ma = 2	Ma = 4	Ma = 4	Ma = 4
Re ≈ 780	Re ≈ 1800	Re ≈ 5400	Re $\approx 4.8 \times 10^4$
Kn $= 2.78 \times 10^{-3}$	Kn $= 2.09 \times 10^{-3}$	Kn $= 7.33 \times 10^{-4}$	Kn $= 8.25 \times 10^{-5}$
Ma/$\sqrt{\text{Re}} = 7.2 \times 10^{-2}$	Ma/$\sqrt{\text{Re}} = 9.4 \times 10^{-2}$	Ma/$\sqrt{\text{Re}} = 5.4 \times 10^{-2}$	Ma/$\sqrt{\text{Re}} = 3.0 \times 10^{-2}$

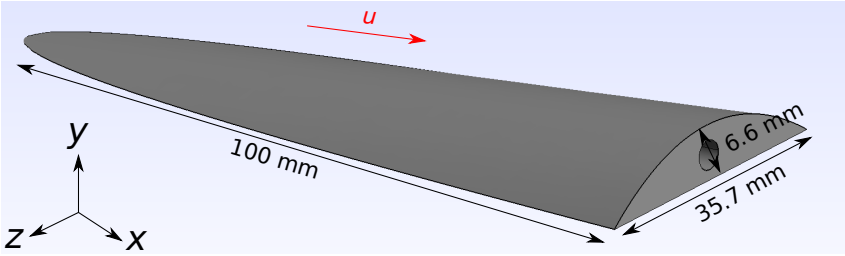

Fig 3. Schematic of the studied waverider model.

fit within MARHy's test section. The model, depicted in Fig. 3 with its dimensions, was 3D-printed in resin. Its base is directly connected to an aerodynamic force balance suited for low-density flows: it was therefore designed to measure lift and drag forces from 1 mN to 1 N. This balance is connected with a rotating arm enabling to vary the angle of attack (AoA) of the waverider model. Therefore, measurements of lift and drag forces are performed at several AoAs for each of the four operating conditions.

In the framework of the APHYRA project, measurements of aerodynamic forces, wall conditions (pressure, temperature, fluxes) and flow properties (pressure, density) are to be performed at several AoA within the hypersonic rarefied wind tunnel MARHy. Numerous freestream Mach numbers (from 2 up to 20.2) and pressures (from 0.068 Pa to 71 Pa) will be considered to vary both Reynolds and Knudsen numbers and thus emulate the conditions that waveriders may be confronted with. At the moment, only force measurements and flow visualisation at Mach numbers of 2 and 4 were performed.

3.2. Description of the 3 super-/hypersonic flow solvers

3.2.1. Theoretical background: rarefied gas flow modelling

Contrary to continuous media that can be described with the Navier-Stokes equations, rarefied media require suitable microscopic description. The relevant mathematical modelling for such a description is the Boltzmann equation. Assuming a dilute flow of mono-atomic gas without external force, this equations can be written as:

$$\partial_t f + \underline{v}.\underline{\nabla_x} f = Q(f, f)\,, \tag{1}$$

where f denotes the mass distribution function. The left-hand side of eq. (1) represents the free flight of the gas molecules while the right-hand side corresponds to the collision kernel. This term has an integral form with a quadratic integrand. The collision kernel is thereby mainly responsible for the complexity to solve the Boltzmann equation.

To overcome this difficulty, several simplified models were proposed in the literature and are commonly

used in the rarefied gas community [9]. Bhatnagar, Gross and Krook [10] introduced the so-called BGK model, where the Boltzmann collision kernel is replaced by a relaxation term towards the local Maxwellian equilibrium distribution $\mathcal{M}[f]$ [1]. This model can then be written as:

$$\partial_t f + \underline{v}.\underline{\nabla_x} f = \frac{1}{\tau}\left(\mathcal{M}[f] - f\right) , \tag{2}$$

where $\tau = \mu/p$ denotes the relaxation time towards the equilibrium. This model satisfies the local conservation laws as well as the local entropy dissipation inequality (H-theorem). The BGK model however suffers from one main limitation: by design, it imposes a Prandtl number of $\mathrm{Pr} = 1$, which is not physically correct.

This limitation was alleviated by Holway [11] who introduced the ES-BGK model (for Ellipsoidal Statistics BGK). In this formulation, the collision term is replaced by a relaxation towards a Gaussian distribution $\mathcal{G}[f]$ [2]rather than a Maxwellian one, that is:

$$\partial_t f + \underline{v}.\underline{\nabla_x} f = \frac{1}{\tau}\left(\mathcal{G}[f] - f\right) , \tag{3}$$

where the relaxation time writes $\tau = \mu(1-\nu)/p$. $\nu \in [-1/2, 1[$ is an additional parameter introduced by the Gaussian distribution $\mathcal{G}[f]$ and used to adjust the value of the Prandtl number given by the following relation:

$$\frac{2}{3} \leq \mathrm{Pr} = \frac{1}{1-\nu} < \infty . \tag{4}$$

For polyatomic gases, the Prantdl number writes:

$$\frac{2}{3} \leq \mathrm{Pr} = \frac{1}{1-\nu(1-\theta)} < \infty , \tag{5}$$

where θ is directly related to the rotation number Z_{rot} by $\theta = 1/Z_{rot}$. As the BGK model, ES-BGK satisfies the conservation laws and the entropy inequality [12].

3.2.2. The Navier-Stokes solver "NS"

The first numerical software employed in the present work is the CEA 3D compressible Navier-Stokes solver denoted *NS*. This in-house code resolves the Navier-Stokes equations on multi-block structured meshes using a finite-volume linearised implicit scheme and a CFL marching step technique.

3.2.3. The deterministic kinetic solver "K"

The CEA 3D kinetic solver called *K* was developed following the work of Mieussens [13]. It was designed to provide a steady-state solution of both BGK and ES-BGK models for mono- and polyatomic gases using a discrete velocity deterministic approach. Mass distribution functions are hence discretised for both spatial and velocity coordinates. The *K* solver requires multi-block structured meshes for spatial discretisation while the velocity grid can be either cartesian or locally refined using an AMR (*Adaptive Mesh Refinement*) algorithm. This AMR strategy was developed by Baranger *et al.* [14] and was shown to provide significant reduction of computational costs.

Spatial integration is performed using a 2^{nd} order finite volume scheme and time integration using a similar linearised implicit scheme as for the *NS* solver. Moreover, a hybrid MPI/OpenMP parallelisation strategy was developed to handle calculations with large computational cost. Finally, a converged *NS*

[1] The Maxwellian distribution writes $\mathcal{M}[f] = \dfrac{\rho}{(2\pi RT)^{3/2}} \exp\left(-\dfrac{|v-u|^2}{2RT}\right)$, where v denotes the molecular velocity vector and u is the flow velocity vector.

[2] The Gaussian distribution writes $\mathcal{G}[f] = \dfrac{\rho}{\sqrt{2\pi \underline{\underline{\mathcal{T}}}}} \exp\left(-\dfrac{1}{2}(v-u).\underline{\underline{\mathcal{T}}}^{-1}.(v-u)\right)$, where $\underline{\underline{\mathcal{T}}}$ is a corrected tensor in which the parameter ν (as well as θ for polyatomic gases) appears.

result is generally used to initialise a *K* computation, performed on the same spatial mesh. Temperature and velocity fields from the continuous solution are used to build the AMR discrete velocity grid, that fits mass distribution function heterogeneities. This was shown to induce a substantial decrease of the number of iterations needed before reaching steady-state conditions [14]. As a consequence, even though the discrete-velocity deterministic approach may be very costly since a 6D space-velocity space is discretized, but the hybrid parallelisation, the initialisation with a *NS* pre-simulation and the velocity-grid AMR algorithm still enable to handle large 3D cases with acceptable computational times.

The in-depth description of the *K* solver is out of the scope of the present paper; extensive details can be found in [14].

3.2.4. The DSMC kinetic solver "SPARTA"

The final numerical code considered in the present study is the well-known SPARTA solver. This open-source platform is developed since 2012 at Sandia National Laboratories by Plimpton *et al.* [15]. This solver makes use of Bird's DSMC (*Direct Simulation Monte Carlo*) algorithm [2] to solve the Boltzmann equation. This stochastic technique is one of the most popular methods for rarefied flows simulations [16]. Briefly, DSMC consists of a way to emulate the physics modeled by the Boltzmann equation by following a representative sample of numerical particles through the flow, each of them representing a large amount of physical atoms or molecules.

3.3. Description of the calculations

The calculations performed with the 3 solvers were carried out on the EXA supercomputer of CEA composed of around 880000 CPUs. For each solver, we took advantage of the symmetry of the waverider model wrt to the xy plane to reduce the size of the computational domain. For each calculation, the limits of the computational domains were set far enough from the obstacle to ensure desired free-stream conditions and supersonic conditions are reached at the outflow boundaries, to avoid any information traveling inward the domain. In the present study, only the three Mach 4 flow conditions, listed in Tab. 1, and 2 AoA (0° and 20°) are considered.

3.3.1. Calculations with the NS and K solvers

As previously described, *K* solver's simulations were initialised from the results of a *NS* calculation. Both solvers were run using the same multi-block structured meshes. Fig. 4 shows a representation of the hexaedral grid of 1.5 million cells built using the ICEM-CFD software. To reduce the meshing effort, only one mesh is considered for the 3 flow conditions and the 2 AoA. Nevertheless, it was ensured that the minimum mesh size in the wall normal direction was maintained around $\Delta y^+ \sim 1$.

CFD computations with the *NS* solver were first performed. A second-order HLLE scheme associated with a Minmod limiter was used for spatial discretisation, and a linearised implicit scheme was employed for time integration. The flow was assumed laminar. Finally, a non-catalytic wall with a fixed temperature $T_w = 293.15$ K was considered. Note that a mesh convergence study was conducted with the *NS* code but is not detailed for concision purpose.

Kinetic computations were then performed with the *K* code on the same spatial grid. The ES-BGK equations were solved using a second-order scheme for spatial discretisation. A linearised implicit scheme was employed for time integration with a CFL marching step technique to speed up convergence. Convergence was usually reached after a few hundred iterations. The flow of air was assumed to be composed of 76 % of N_2 and 24 % of O_2. Using eq. (5) with $\nu = -0.5$ and $\theta = 0.2$, the Prandtl number was fixed at Pr $= 0.714$. Furthermore, vibrations and chemical reactions were neglected. The rotation mode was accounted for, with a constant relaxation number $Z_{rot} = 5$. The Maxwell gas-surface interaction model was employed and full thermal accommodation was assumed at the wall, that is $\alpha_{\text{acc}} = 1$. An AMR velocity grid refinement was used to reduce the overall computational cost. A convergence study wrt the velocity grid was performed and is not described in the present paper for the sake of conciseness.

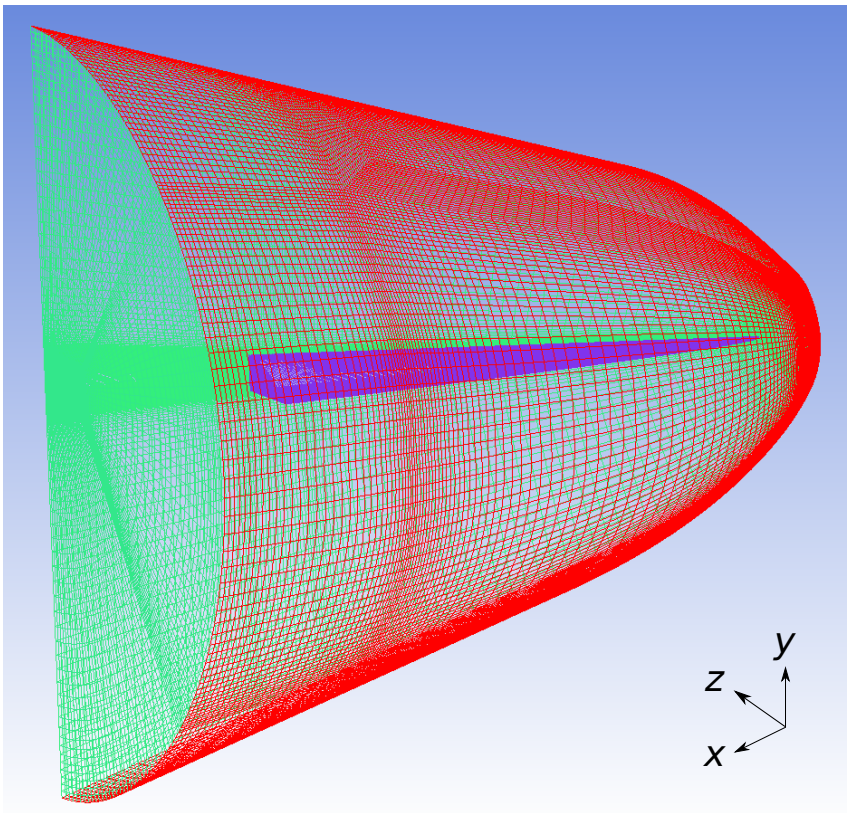

Fig 4. Representation of the multi-block structured mesh used for the *NS* and *K* computations. Inflow conditions are imposed on the red boundary.

3.3.2. Calculations with SPARTA

The DSMC simulation parameters are summarised in Tab. 2 and detailed hereafter. 3D computations were performed within a 0.15 m $\times$ 0.12 m $\times$ 0.1 m (L $\times$ H $\times$ l) box. The physical parameters (gas composition, gas/surface interaction, wall temperature, internal mode and chemical reactions modelisation) are similar with the *K* simulations. Regarding the particles' collision, the VSS (Variable Soft Sphere) model of Koura and Matsumoto [17] was employed with Bird's standard parameters (Appendix A of [2]). Furthermore, the NTC (No Time Counter) algorithm of Bird was used for the choice of collision partners. The particles density of the inflow gas N_ρ, the ratio of physical particles to numerical particles number f_{num} and the number of particles N_{part} within the computational domain are given in Tab. 2 for each flow condition. Finally, to ensure to satisfactorily capture the flow physics:

- the time step Δt is always chosen smaller than the time τ_{coll} needed by the particles to travel the mean free path distance;
- the number of numerical particles per cell $N_{\text{p/c}}$ is fixed to 20 to ensure to compute statistically reliable flow quantities;
- the cell size must be smaller than the local mean free path to avoid any particle to interact with another further than this distance, which is ensured by a $200 \times 150 \times 125$ initial grid and a 3-levels AMR refinement.

Table 2. Physico-numerical SPARTA simulation parameters.

Parameters	M4-2.67Pa	M4-8Pa	M4-71Pa
$N_\rho = \rho/m_{\text{gas}}$	2.77×10^{21}	8.31×10^{21}	7.39×10^{22}
f_{num} $[-]$	4×10^{10}	9×10^{10}	1×10^{12}
N_{part} $[-]$	$\sim 10^8$	$\sim 10^8$	$\sim 10^8$
Δt [s]	1×10^{-7}		1×10^{-8}
$\tau_{\text{coll}}/\Delta t$ $[-]$	5	1.8	1.98
Gas composition	$\chi_{N_2} = 0.76$, $\chi_{O_2} = 0.24$		
Gas/surface	Maxwell model – $\alpha_{\text{acc}} = 1$		
Wall temperature	$T_w = 273.15$ K		
Collision model	VSS [17]		
Rotation	$Z_{rot} = 5$		
Vibration	None		
Chemical reactions	None		
Initial spatial grid	$200 \times 150 \times 125$		
Final spatial grid	3-levels AMR refinement		
$N_{\text{p/c}}$ $[-]$	20		

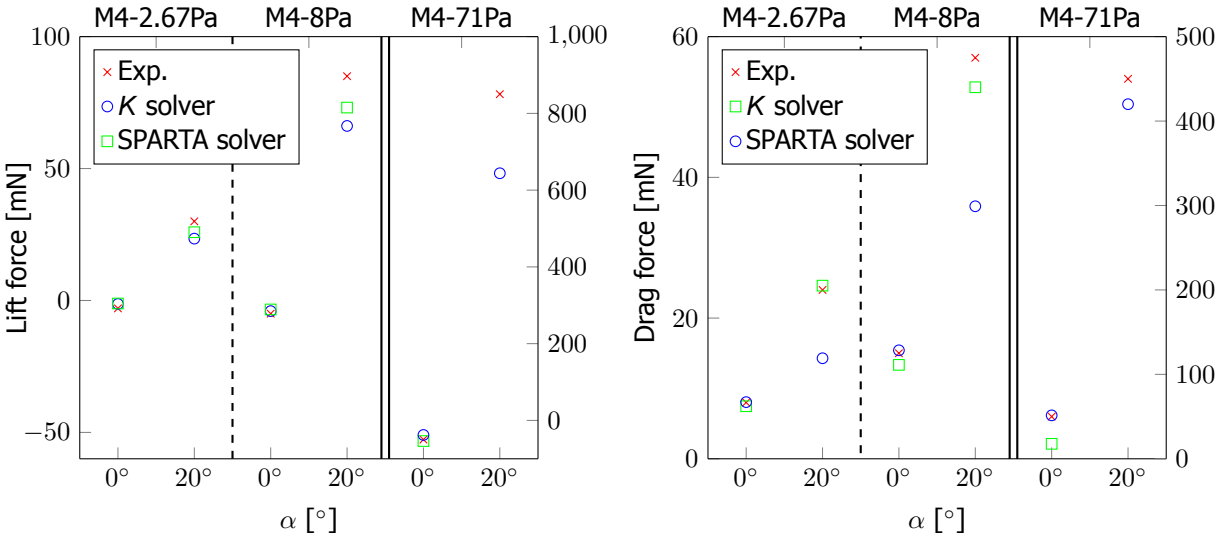

(a) Lift force **(b)** Drag force

Fig 5. Comparison between the experimental and numerical (a) lift force and (b) drag force. For each graph, the y coordinate is on the left for the M4-2.67Pa and M4-8Pa cases and on the right for the M4-71Pa flow condition.

4. Results and discussion

Before examining in details the numerical results, their relevance is first assessed. This is performed by comparing the simulation's results with the experimental data. Then some solver-to-solver comparisons are performed.

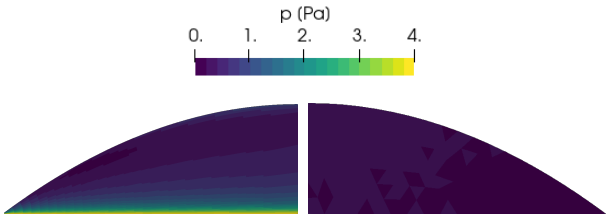

Fig 6. Contours of static pressure on the base of the waverider captured by *K* (left) and SPARTA (right) for the M4-2Pa flow conditions and 20° AoA.

4.1. Comparison with experimental data

Fig. 5 shows the comparison of the lift $\overrightarrow{L}$ and drag $\overrightarrow{D}$ forces measured by CNRS/ICARE for the three Mach 4 flow conditions and the two AoA considered (0° and 20°) with the forces computed numerically. In a xy cartesian coordinate system, these forces can be decomposed as follows:

$$\begin{array}{rl} \overrightarrow{L} & = F_y \cos(\alpha) - F_x \sin(\alpha) \\ \overrightarrow{D} & = F_x \cos(\alpha) + F_y \sin(\alpha) \end{array} , \tag{6}$$

where α denotes the AoA and F_x and F_y the sum of pressure and contributions efforts in the x and y direction, i.e.

$$\begin{array}{rl} F_x & = \displaystyle\int_S -p\, n_x \, ds + \int_S \overrightarrow{\tau_w}.\overrightarrow{x} \, ds \\ F_y & = \displaystyle\int_S -p\, n_y \, ds + \int_S \overrightarrow{\tau_w}.\overrightarrow{y} \, ds \end{array} , \tag{7}$$

with n_x, n_y the unit normal of the body surface in the x, y direction pointing to the fluid and $\overrightarrow{\tau_w}$ refers to the wall viscous shear stress.

From the fields of pressure and wall shear stress on the body surface, the total forces are easily computed. As illustrated in fig. 5, satisfactory agreement is noticed between the experimental data and the numerical estimation of the lift force by *K* and SPARTA. Both solvers provide very close estimations of lift force and tend to slightly underestimate the lift force as the AoA increases. However, contrary to the *K* solver, SPARTA significantly underestimates the value of the drag, especially at 20° AoA. This is mainly due to an underestimation of the pressure field on the base surface compared to the *K* simulation, as shown in Fig. 6. This observation may be explained by the lack of particles in the base-flow region, which is highly rarefied. Note however that without the base contribution, *K* solver and SPARTA provide very close estimation of the drag force, which highlight the consistency between the two solvers.

4.2. Comparison of the 3 solvers for a given study case

The M4-2.67Pa and 20° AoA case is chosen to perform some solver-to-solver comparisons. Fig. 7 shows the contours of static pressure computed by the *NS*, *K* and SPARTA solvers in the xy symmetry plane of the waverider. Very similar pressure fields are provided by the three solvers below the lower surface of the waverider. Contrary to the SPARTA mesh which is refined with respect to the local density and therefore particularly refined in the vicinity of the shock, the *NS* and *K* is not fully adapted to the shape of the shock. However, as shown in Fig. 7, this does not significantly affect the estimation of the aerodynamic properties of the waverider. This observation is reinforced by Fig. 8, which depicts the contours of static pressure on the lower surface of the waverider. Very close pressure fields are captured by the 3 solvers over the lower surface, which is expected to strongly contribute to the lift force, especially when the waverider has positive AoA.

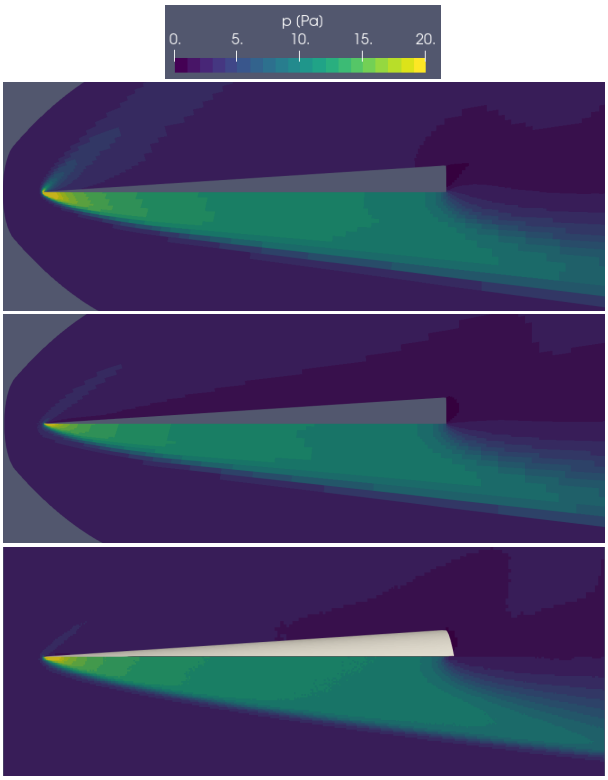

Fig 7. Contours of static pressure in the xy symmetry plane captured by *NS* (top), *K* (middle) and SPARTA (bottom) for the M4-2Pa flow conditions and 20° AoA (the freestream flow goes from the bottom left to the top right).

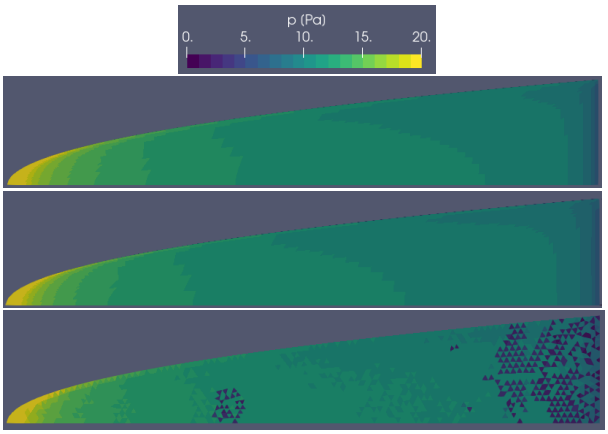

Fig 8. Contours of static pressure over the lower surface of the waverider captured by *NS* (top), *K* (middle) and SPARTA (bottom) for the M4-2Pa flow conditions and 20° AoA.

5. Conclusion

The present work took advantage of the experimental measurements of CNRS/ICARE in the framework of the ANR APHYRA project to numerically study the aerodynamic properties of a waverider designed from a conical flowfield. Simulations with a Navier-Stokes, a discrete ordinate ES-BGK and a DSMC solvers were performed for 3 flow conditions (M4-2.67Pa, M4-8Pa and M4-71Pa), spanning both continuous and rarefied slip regimes, and 2 AoA (0° and 20°). Satisfactory agreement was observed between numerical and experimental results, except regarding the estimation of the drag force by SPARTA for which a significant underestimation of the pressure level is noticed in the base-flow region due to a lack of particles in this zone. The results introduced in the present paper are only the beginning of a more extensive numerical analysis, that may complement the experimental findings of CNRS/ICARE. Interesting future development may involve to extend the present analysis to more AoA, that were already experimentally addressed by CNRS/ICARE. Note also that the present study will be complemented by new experimental measurements of CNRS/ICARE (measurements of wall – pressure, temperature, fluxes – and flow conditions – density) at the Mach 2 and 4 flow conditions, but also under hypersonic conditions (Mach 20). First numerical simulations at Mach 20 are already in progress.

References

[1] T. R. F. Nonweiler, "Delta wings of shape amenable to exact shock wave theory," *Journal of Royal Aeronautical Society*, vol. 67, pp. 39, 1963.

[2] G. A. Bird, *Molecular Gas Dynamics and the Direct Simulation of Gas Flows*, Oxford University Press, New York, 1994.

[3] F. Ding, J. Liu, C. Shen, Z. Liu, S. Chen, and X. Fu, "An overview of research on waverider design methodology," *Acta Astronautica*, vol. 140, pp. 190–205, 2017.

[4] J. D. Anderson, *Hypersonic and High Temperature Gas Dynamics – Second Edition*, AIAA, 2006.

[5] X. He and M. L. Rasmussen, "Computational analysis of off-design waveriders," *Journal of Aircraft*, vol. 31, pp. 345–353, 1994.

[6] H. Noubel and V. Lago, "Experimental analysis of waverider lift-to-drag ratio measurements in rarefied and supersonic regime," *IntechOpen*, 2021.

[7] D. Toussaint, H. Noubel, C. Baranger, J.-P. Braeunig, and V. Lago, "Influence of rarefaction degree and aft-body geometry on supersonic flows," *In submission process*, 2022.

[8] T. C. Rolim, P. G. de Paula Toro, M. A. S. Minucci, A. de Carlos de Oliveira, and R. da Cunha Follador, "Experimental results of a Mach 10 conical-flow derived waverider to 14-X hypersonic aerospace vehicle," *J. Aerosp. Technol. Manag.*, vol. 3, pp. 127–136, 2011.

[9] L. Mieussens, "A survey of deterministic solvers for rarefied flows," in *Proccedings of the 29th International Symposium on Rarefied Gas Dynamics*, 2014.

[10] P. L. Bhatnagar, E. P. Gross, and M. Krook, "A model for collision in gases. I. Small amplitude processes in charged and neutral one-component systems.," *Phys. Rev.*, vol. 94, pp. 511–525, 1954.

[11] L. H. Holway, "Kinetic therory of shock structure using an ellipsoidal distribution function," in *Rarefied Gas Dynamics*, New York Academic Press, Ed., 1966, vol. 1, pp. 193–215.

[12] P. Andries, P. Le Tallec, J.-P. Perlat, and B. Perthame, "The Gaussian-BGK model of Boltzmann equation with small Prandtl number," *European Journal of Mechanics / B Fluids*, vol. 19, pp. 813–830, 2000.

[13] L. Mieussens, *Modèles à vitesses discrètes et méthodes numériques pour l'équation de Boltzmann-BGK*, Ph.D. thesis, Université Bordeaux I, 1999.

[14] C. Baranger, J. Claudel, N. Hérouard, and L. Mieussens, "Locally refined discrete velocity grids for stationary rarefied flow simulations," *Journal of Computational Physics*, vol. 257 (15), pp. 572–593, 2014.

[15] S. J. Plimpton, S. G. Moore, A. Borner, A. K. Stagg, T. P. Koehler, J. R. Torczynski, and M. A. Gallis, "Direct simulation Monte Carlo on petaflop supercomputers and beyond," *Physics of Fluids*, vol. 31, no. 086101, 2019.

[16] E. Josyula and J. Burt, "Review of rarefied gas effects in hypersonic applications," Tech. Rep., OTAN, 2011.

[17] K. Koura and H. Matsumoto, "Variable Soft Sphere molecular model for inverse-power-law or Lennard-Jones potential," *Physics of Fluids*, vol. 3, pp. 2454, 1991.